Destabilization of olivine by 30-keV electron irradiation: A possible mechanism of space weathering affecting interplanetary dust particles and planetary surfaces

L. Lemelle,[1,*] L. Beaunier,[2] S. Borensztajn,[2] M. Fialin,[3] and F. Guyot[4]

[1]Laboratoire de Sciences de la Terre, Ecole Normale Supérieure de Lyon, UMR5570, 46 allée d'Italie, 69364 Lyon Cedex 07, France
[2]Laboratoire de Physique des Liquides et Electrochimie, case 133, 4 place Jussieu, 75252 Paris Cedex 05, France
[3]Service de Microanalyse CAMPARIS-CNRS, Université Pierre et Marie Curie, case 110, 4 place Jussieu, 75252 Paris Cedex 5, France
[4]Laboratoire de Minéralogie et Cristallographie de Paris, case 115, and IPGP, 4 place Jussieu, 75252 Paris Cedex 05, France

Abstract—Electron irradiation experiments were performed using a 30-keV electron beam on single crystals of olivine in a scanning electron microscope (SEM) and in an electron microprobe (EMP). We determined that, under certain conditions, structural damage is caused to the irradiated surface of iron-bearing olivines. The irradiated areas comprise spherules with sizes of hundreds of nanometers and micrometer-sized holes. In the immediate vicinities of the irradiated areas, droplets with sizes of tens of nanometers and branching tracks are observed. With increasing total charge, the hundreds of nanometer-sized spherules become larger and more irregular in shape. The size and shape of the nanometer-sized droplets remain almost constant, but their surface density increases (in m^{-2}). Chemical fractionations compared to the initial olivine were found: the irradiated areas are slightly enriched in MgO, whereas the deposits are enriched in SiO_2. Destabilization of olivine is not due to the dissipation of the implanted energy as heat, but results most probably from electrostatic discharges leading to the breakdown of the dielectric lattice. The possibility that such processes could be responsible for significant space weathering of interplanetary dust particles and regoliths of planetary surfaces should be taken into account. In the interplanetary medium, 10-keV range electrons are carried by the solar wind, whereas at 1 AU from the Sun, the lifetime of cometary dust and the exposure time of lunar regolith are, at least, 10 to 100 times greater than the duration required to accumulate the damaging electronic doses applied in this study. Moreover, the comparison of the microstructures of samples irradiated in the present study with features of lunar regolith grains reveals several chemical and structural similarities.   *Copyright © 2003 Elsevier Science Ltd*

1. INTRODUCTION

Space weathering is due to a family of processes active in the space environment, such as heating, micrometeorite impacts, stellar winds, or cosmic ray irradiation, which combine to alter the physical and/or compositional properties of space materials (Pieters, 1998). The identification of a prevailing process, if any, is important for interpreting planetary surface properties, as well as the bulk composition of dust particles. The study of space weathering in the interplanetary medium benefits from the constraints obtained from investigations of both space-weathered lunar samples (Keller and McKay, 1997) and of the solar wind (Reames, 1999). Direct implications concern bodies of the solar system devoid of atmosphere, including interplanetary dust particles and cometary dust (Brownlee, 1985; Jessberger et al., 1988; Bradley et al., 1989; Hanner et al., 1994; Crovisier et al., 1997; Wooden et al., 1999), as well as asteroidal and lunar surfaces.

Numerous experiments have shown specific structural and chemical effects of irradiation on silicates by one kind of charged species present in the solar wind. Irradiation with MeV protons or helium or krypton cations induces the formation of nuclear tracks and of amorphous surfaces having higher O/Si ratios than in the bulk (Bibring et al., 1972; Wang et al., 1991; Bradley, 1994). It has also been shown that proton irradiation of olivine leads to lower Mg/Si ratios (Bradley, 1994). Mechanisms previously proposed to describe lattice damage include physical processes that are critically dependent on the cation mass. Irradiation with keV protons, helium and argon cations may modify the chemical composition and the microstructure of the silicate surface (Hochella et al., 1988; Demyk et al., 2001). The reduction of iron and silicon cations in olivine by protons was suggested by Dukes et al. (1999). Irradiation with 100-keV range electrons generates the formation of amorphous rims in silicates (e.g., beryl, cordierite, nepheline, sphene; see Vance et al., 1986; Gong et al., 1998). The breakdown of olivine into associated MgO crystallites and an amorphous SiO_2-rich phase, with a lower Mg/Si ratio than the initial olivine was reported by Carrez et al. (2001).

Among possible irradiation processes, the irradiation by 10-keV range electrons from the solar wind (Lin et al., 1997; Krucker et al., 1999) is considered in this paper. Our aim was to investigate the chemical and structural response of olivine, an ubiquitous phase in the solar system, subjected to 30-keV electrons. Natural San Carlos olivine and synthetic iron-free forsterite single crystals were irradiated with various electron doses in a scanning electron microscope (SEM) and in an electron microprobe (EMP). Microstructures and chemical compositions of the samples were then analyzed by both SEM and EMP. The most extensively studied case of space weathering is the one affecting grains of the lunar regolith (Keller and McKay, 1997), subjected both to solar wind and to micrometeoritic impacts. A fruitful approach to discuss the mechanism

---

* Author to whom correspondence should be addressed (llemelle@ens-lyon.fr).

Table 1. EMP analyses of the samples prepared during experiment #13 (Table 2). Descriptions of the analytical procedures are given in text.

Major elements	Initial olivine		Deposit		Irradiated olivine			
	wt%[a]	at%	at%[b]	corrected at%[c]	wt%[d]	ρ[e]	corrected wt%[f]	corrected at%[g]
O	43 (2)[h]	57.0	59.6 (2)	58.9	40.3 (4)	1.095	44	57.6
Si	18.8 (2)	14.2	19.4 (3)	17.8	17.75 (2)	1.028	18.3	13.7
Mg	29.4 (2)	25.65	17.2 (5)	19.3	28.5 (2)	1.048	29.9	25.8
Fe	8.3 (2)	3.1	3.7 (6)	4.04	7.4 (1)	1.055	7.8	2.9
Total	99.5		99.9		93.95		100	

[a] Average composition of 20 EMP analyzes of starting olivine.
[b] Average composition of 32 EMP raw analyzes of the deposit formed on the graphite substrate.
[c] Composition obtained from column b by the STRATA program.
[d] Average composition of 15 EMP analyzes of an irradiated olivine.
[e] Correction parameters for rugosity (Fig. 8).
[f,g] Composition obtained from column d after correction of rugosity effects.
[h] Errors calculated on the basis of statistical precision of analyzes are given in parentheses.

of space weathering is to compare space-weathered samples to samples artificially processed in the laboratory. This has already been done for ions with solar wind energies (Bibring et al., 1972; Bradley, 1994) and for interplanetary dust impacts (Hiroi and Sasaki, 2001; Sasaki et al., 2001). Similarities between microstructures observed in lunar regolith and those in our samples are discussed.

2. EXPERIMENTAL

2.1. Sample Preparation

Two centimeter-sized single crystals were used in this study: a natural olivine and a pure synthetic Mg_2SiO_4 forsterite. Both crystals were oriented with a precision of $\pm 2°$ using the Laue X-ray technique. The natural San Carlos olivine, of gem quality, was selected for its optical quality. The initial olivine material, analyzed by EMP, is an $(Mg_{0.89}Fe_{0.11})_2SiO_4$ olivine (analysis with no minor elements reported in Table 1). Oriented slices of both samples with dimensions 1.8 mm × 2.2 mm × 0.7 mm were cut parallel to the (010) surface (Pbnm configuration of space group #62). Polishing of the crystals was carried out manually on the two (010) surfaces, using fine diamond powders on silk, and was completed with a diamond powder with 0.25 μm average grain size.

After irradiation, two types of cross-sections of the irradiated areas were prepared by mechanical polishing. One was obtained from samples embedded in an epoxy resin, the other one from samples that were not embedded.

2.2. Irradiation Experiments

The iron-bearing and iron-free olivines, without conductive coating, were placed in the vacuum chambers ($p = 10^{-6}$ bar in both SEM and EMP). 100 × 100 μm^2 surfaces were continuously rastered with a 30-kV, 60-nA (measured with a Faraday cage) focused electron beam. The irradiation procedure was studied by varying three parameters: the period of scanning, T (in s); the density of charges deposited per surface unit and per scan, Q (pCμm^{-2}); and the total time of irradiation of a single surface area, t (min). We note that in these irradiation experiments, the period of scanning is linearly related both to the time elapsed between two subsequent occurrences of the beam at a same point, and to the duration of irradiation at each point. A summary of experiments and irradiation conditions is given in Table 2.

In some of the irradiation experiments, a graphite "witness plate" was attached to the sample holder in contact with the olivine, perpendicular to its surface, to collect material emitted from the olivine during electron bombardment. After irradiation, the graphite was removed from the sample holder, and the graphite surface was studied by SEM and EMP.

2.3. Sample Characterization

To study both structural and chemical changes induced by the electronic irradiation, recovered damaged olivines and cross-sections were coated with a thin 10-nm amorphous graphite layer to avoid charging. The microstructures were first imaged at 20 keV with secondary electrons (SE) in a Stereoscan 440 (Leo) SEM. This SEM has a 4.5-nm resolution and a 10-nm probe size; the strong SE contrast generated by small particles on very flat surfaces allows one to image particles with diameters smaller than the electron probe beam diameter. Chemical compositions were then studied with a Cameca SX 50 EMP operated at 5 keV and 10 keV. First-order reflection of K emission lines was analyzed with a spectrometer equipped with two different monochromators, namely a TAP (1011) for MgK_α and SiK_α and a W/Si multilayer crystal for OK_α and FeL_α. The analytical standard for EMP analyses was a 10% fayalite-containing olivine (Lemelle et al., 2000). Data reduction for matrix effects was carried out with a "$\phi(\rho z)$" procedure (Pouchou and Pichoir, 1984). The average chemical compositions of the deposits collected on the graphite surface were also studied by EMP, but data reduction was carried out with a thin film software known under the commercial denomination STRATA (Pouchou and Pichoir, 1991). Over the past 15 yr, it has been developed into a powerful tool to quantify both chemical compositions and thicknesses of thin layers deposited on bulk substrate. The detection limits can be determined, for the present state of instrument technology and correction model theory, to be 10^{14} to 10^{15} atom/cm^2, i.e., less than one atomic monolayer, provided that the layer and the substrate have no common elements (Karduck, 1998). For complicated problems (e.g., more than one deposited layer, presence of a same element in more than one layer), the analytical protocol consists of performing measurements at different beam electron energies for the method to be successfully applied (Willich and Wishmann, 1998). In the present study, a single layer of silicate was deposited on a bulk carbon substrate offering a rather simple system that can be studied at a single beam energy. We selected an accelerating voltage of 5 kV to excite with sufficient efficiency the most energetic of the measured X-ray lines, i.e., Si Kα (excitation threshold: 1.83 keV). It is common practice in electron probe microanalysis to set the beam energy at least 3 times higher than the excitation threshold to maximize intensities.

3. RESULTS

3.1. Microstructural Effects

The initial planar surfaces of Fe-bearing olivine single crystals can be strongly modified by 30-keV electron irradiation, as seen in Figure 1. Irradiated zones are those having secondary electron contrasts brighter than the surrounding unaffected olivine due to more pronounced surface rugosity. By comparison,

Table 2. Summary of experimental conditions of irradiation of iron-bearing olivine (San Carlos olivine $Fo_{89}Fa_{11}$).

#[a]	Effect[b]	T[c] (s)	Q[d] (pC μm^{-2})	F[e] (10^{14} cm^{-2})	t[f] (min)	ΣQ[g] (pC μm^{-2})	i[h] (10^3 pA)	S[i] (μm^2)
1	no	$17\ 10^{-3}$	$4.5\ 10^{-2}$	0.3	30	4765	0.4	50×3
2	no	17.10^{-3}	54.4	337	15	2,880,000	480	50×3
3	no	$17\ 10^{-3}$	54.4	337	30	5,760,000	480	50×3
4	no	30	$1.6 10^{-2}$	0.1	15	0.48	0.05	300×300
5	no	30	0.033	0.2	15	1	0.1	300×300
6	yes	30	0.133	0.8	15	4	0.4	300×300
7	yes	30	133	824	15	3990	400	300×300
8	yes	30	180	1116	1	360	60	100×100
9	yes	30	180	1116	2	720	60	100×100
10	yes	30	180	1116	3,5	1260	60	100×100
11	yes	30	180	1116	5	1800	60	100×100
12	yes	30	180	1116	10	3600	60	100×100
13	yes	30	180	1116	15	5400	60	100×100
14	yes	60	360	2232	15	5400	60	100×100
15	yes	948	5688	35,265	15	5400	60	100×100

[a] Reference number of experiment.
[b] SEM diagnostic of structural damage.
[c] Duration of one scan.
[d] Supplied charge per surface unit during one scan.
[e] Fluence derived from Q by dividing by the electron charge, that is, number of incident electrons per centimeter squared surface area per scan.
[f] Total duration of one experiment.
[g] Total charges supplied per surface unit during the experiment.
[h] Electron beam intensity.
[i] Lengths of each side of the rectangular surface area swept during one scan.

iron-free forsterite single crystals have a very different behavior: no induced structural damage was observed in any of the irradiation experiments conducted on Fe-free olivine in this study.

At the surface of the irradiated areas of Fe-bearing olivine, spherules of diameters of a few hundred nanometers are observed (Figs. 2 and 3a). Their shapes and sizes are regular and specific to each experiment. In all cases, they are homoge-
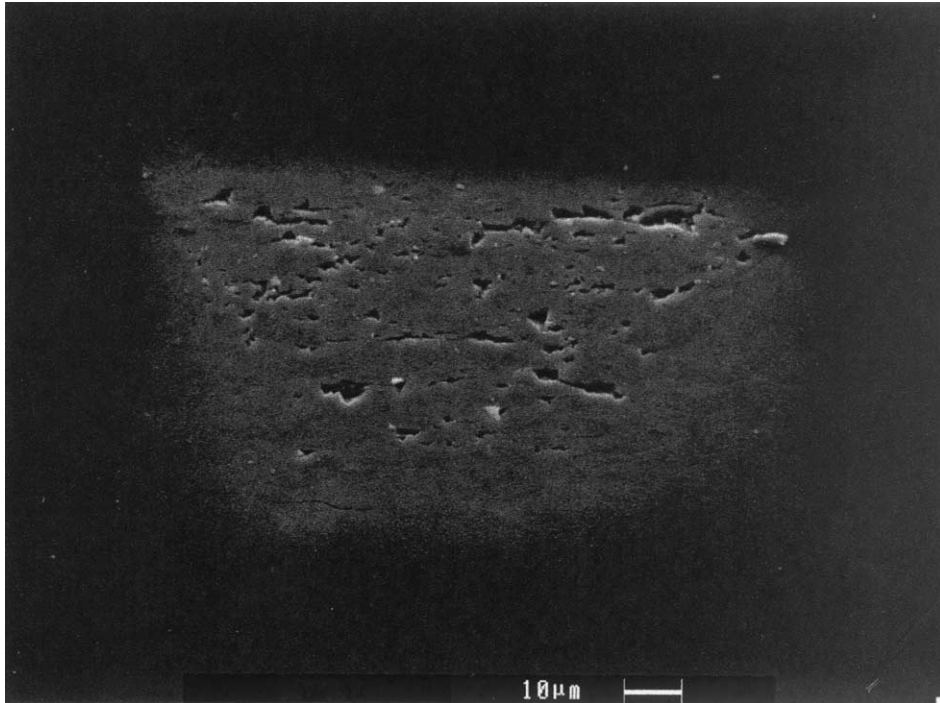

Fig. 1. Secondary electron (SEM) image (tilt angle of 60°) of olivine surface (10% Fa–90% Fo) scanned 4 times on a 100 $\mu m \times 100\ \mu m$ area with a 60-nA beam ($Q_i = 180$ pC/μm^2 and $T = 30$ s). Irradiation parameters are given in Table 2 (#9), and description of the features in text.
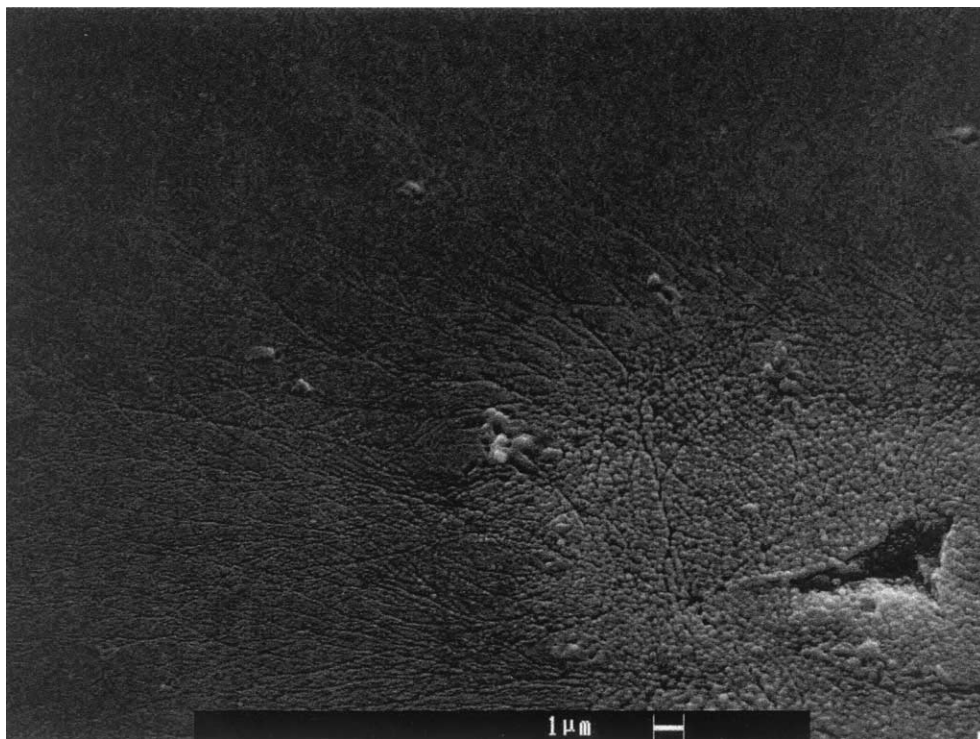
Fig. 2. Secondary electron (SEM) image (tilt angle of 60°) of microstructures observed at the upper left corner of the 100 μm $\times$ 100 μm irradiated zone (10% Fa–90% Fo) shown in Figure 1. Description of features is given in text.

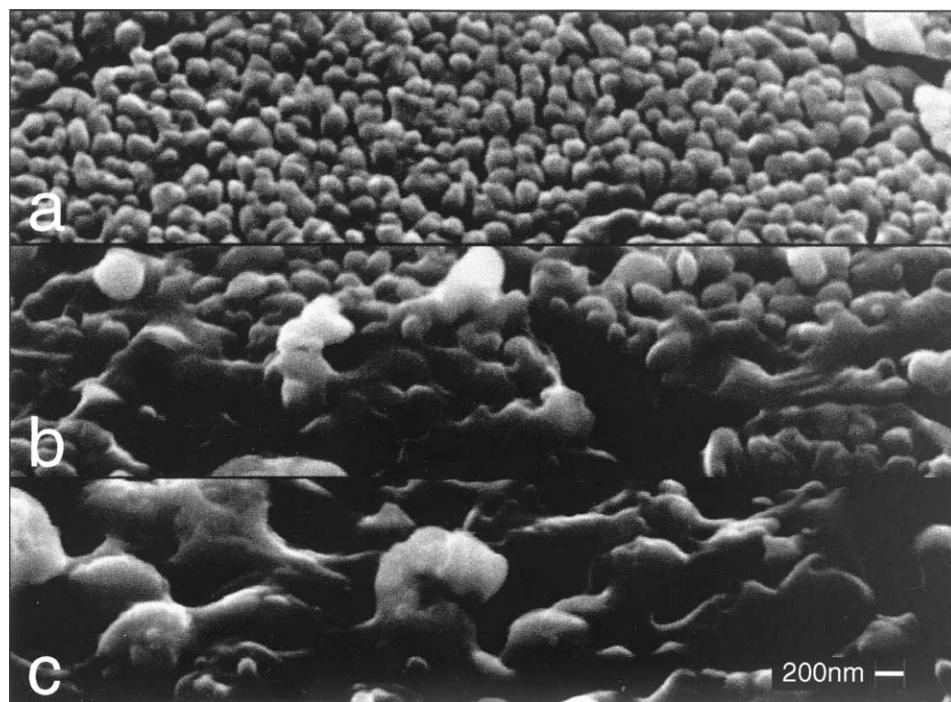Fig. 3. Secondary electron (SEM) images (tilt angle of 60°) of surface microstructures inside 100 μm $\times$ 100 μm irradiated zones, scanned (a) 4, (b) 20, and (c) 30 times (Q_i = 180 pC/μm^2 and T = 30 s). Irradiation parameters are given in Table 2 (#9 for a, #12 for b, #13 for c).
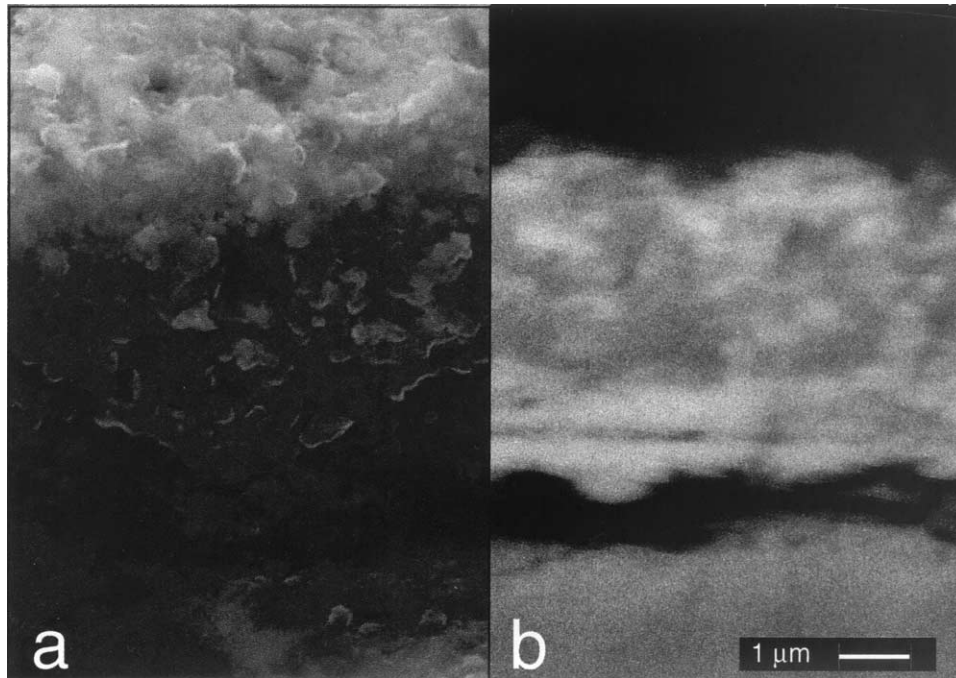
Fig. 4. (a) Secondary electron (SEM) images (tilt angle of 60°) of a cross-section of the 100 μm $\times$ 100 μm irradiated zone of Figure 3 obtained by fracturing. (b) Backscattered electron (SEM) image (not tilted) of a cross-section of the 100 μm $\times$ 100 μm irradiated zone obtained by polishing.

neously distributed and cover the entire irradiated zone. In addition, micrometer-sized holes are present on the surface of the irradiated zones (Figs. 1 and 2). The surface density of the holes is constant at $\sim 10^{-2}$ μm^{-2} for all experiments. The holes exhibit sharp edges, and some are surrounded by micrometer-sized fragments of olivine also showing sharp edges (Fig. 1). SEM observations of cross-sections perpendicular to the irradiated zones reveal a 4- to 5-μm-thick layer presenting structural modifications (Fig. 4). This layer is composed of aggregated spherules (Fig. 4a), and it is separated from the bulk crystal by fractures (Fig. 4b). In the immediate vicinity of the irradiated zone, branching tracks and nanometer-sized droplets are observed (Figs. 2 and 5a). These droplets are ten times smaller than the spherules observed in the irradiated areas, and they have irregular shapes and sizes. They are deposited onto the olivine surface and, in some cases, onto the branching tracks. Surface densities of branching tracks and droplets decrease away from the irradiated zone.

As shown by the comparison between the sets of experiments [#1, #5] to [# 6, #15] (Table 2), two conditions need to be fulfilled simultaneously for producing irradiation microstructures in olivine: 1) the scanning period (T) should be longer than a few seconds, and 2) the supplied charge per surface unit (Q_i in pCμm^{-2}) should be larger than a certain threshold value of some pCμm^{-2}. Note, in addition, that no structural damage was detected either in samples irradiated with long scanning periods and with small supplies of charge (see experiments # 4 and # 5 in Table 2 with $T = 30$ s and $Q < 10^{-2}$ pCμm^{-2}) or in samples irradiated with short scanning periods with large supplies of charge (see experiments #2 and #3 in Table 2 with $T < 10^{-2}$ s and $Q > 10$ pCμm^{-2}). Under appropriate damaging conditions, the other irradiation param-

eters do not control the occurrence of structural damage in olivine but determine their morphologic characteristics. Within the precision of our observations, we note no distinguishable effects (see experiments #13, #14, and #15 and Fig. 6), provided that the total deposited charge (ΣQ in Table 2) is the same. With increasing total charge (see experiments #8 to #13 in Table 2), the surfaces of the irradiated areas become smoother with progressive changes in spherule morphologies. Spherules become larger and more irregular in shape (Fig. 3). In the vicinity of the irradiated zone, densities of braching tracks and ejected droplets increase whereas sizes and shapes of droplets remain almost unchanged (Fig. 5).

3.2. Chemical Effects

In experiments with graphite substrate placed in contact with, and perpendicular to the irradiated zones (Fig. 7 left), the exposed graphite surface was covered with a deposit ejected from the olivine during the electron bombardment. X-ray maps obtained across the coated/uncoated border of the graphite surface reveal the formation of an Si, Mg, Fe, and O deposit due to irradiation of olivine (Fig. 7 right). The average chemical composition of this deposit was studied by EMP at 5 kV. Data reduction was carried out with the STRATA procedure specifically designed for electron probe microanalysis of thin layers deposited on bulk substrate. Results are reported in Table 1. The average thickness of the deposits is estimated to be ~ 10 nm, similar to the observed sizes of droplets at the vicinity of the irradiated surface (Fig. 5). The O/Si and (Mg + Fe)/Si ratios are close to 3.3 and 1.3, indicating a composition of the deposits close to pyroxene, most likely an amorphous/glassy deposit. The Fe/Si ratios of the deposits are close to that of the
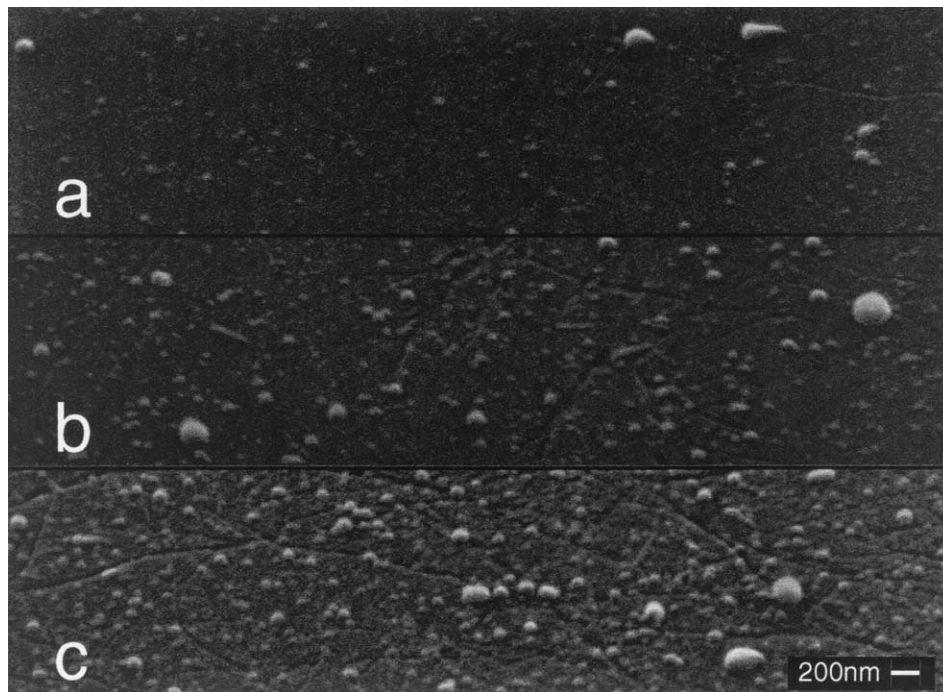
Fig. 5. Secondary electron (SEM) images (tilt angle of 60°) of surface microstructures located 16 μm away from the border of the 100 μm $\times$ 100 μm irradiated zone, scanned (a) 4, (b) 20, and (c) 30 times ($Q_i = 180$ pC/μm^2 and $T = 30$ s). Irradiation parameters are given in Table 2 (#9 for a, #12 for b, #13 for c).
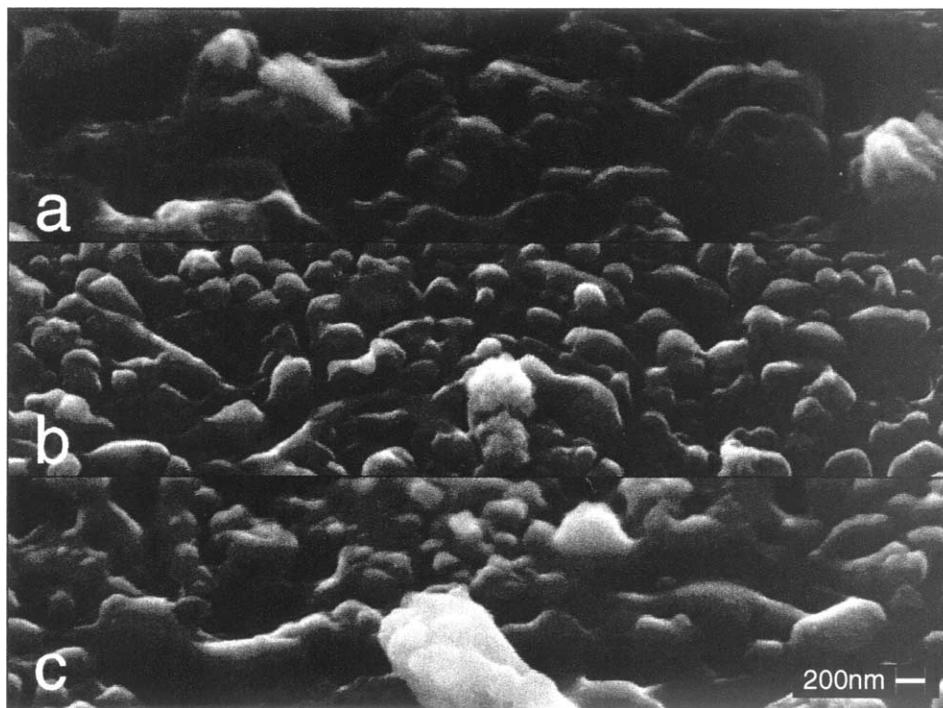

Fig. 6. Secondary electron (SEM) images (tilt angle of 60°) of surface microstructures inside the 100 μm $\times$ 100 μm irradiated zones, scanned in different ways with the same total amount of charge deposited ($\Sigma Q = 5400$ pCμm^{-2}). Irradiation parameters are given in Table 2 (#13 for a, #14 for b, #15 for c).
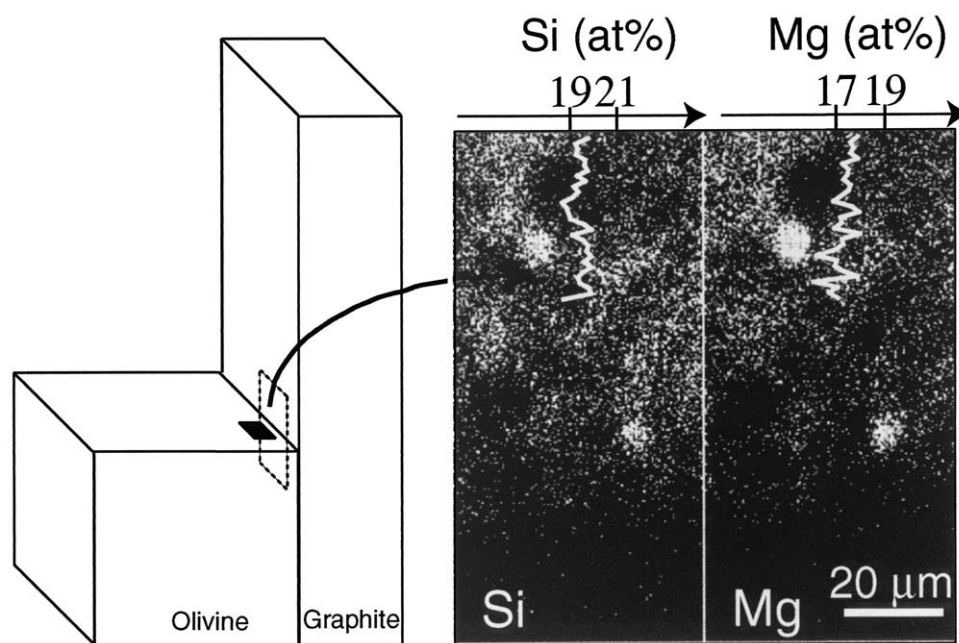
Fig. 7. (left) Schematic illustration of irradiation experiments conducted in the electron microprobe. The 100 μm $\times$ 100 μm irradiated zone is symbolized by the black area. The position of the 100 μm $\times$ 100 μm graphite witness plate is indicated by dotted square. (right) Mg and Si X-ray maps reveal a silica-rich deposit on the exposed graphite. Operating conditions are: 5-kV high voltage, 100-nA beam current, and focused probe ($\sim$ 1 μm diameter). Acquisition times per point are 20 s for Mg, 20 s for Si, and 100 s for Fe. Composition profiles measured on this zone, nontreated with the STRATA program, are represented on the maps.

initial olivine, whereas the Mg/Si ratios are lower. Residual products, slightly enriched in MgO, are probably located in the irradiated area.

Note that the data do not provide any information about the crystallinity of the MgO-rich product. EMP analyses of the irradiated olivine are reported in Table 1. Given the limited depth resolution of the electron microprobe (i.e., 2 to 3 μm), analyses are from mixed contributions of materials, which can be diversely affected by the irradiation. The O/Si and (Mg + Fe)/Si ratios are very close to 4 and 2, respectively, indicating that the layer affected by structural modifications has a chemical composition close to that of an olivine (Fig. 4). Effects of the surface rugosity on the EMP analyses were estimated from an olivine sample with a surface roughened by polishing with abrasives. Figure 8 shows the variations of the elemental compositions of the olivine together with the analytical total: the higher the surface rugosity, the lower the analytical total. From these measurements, a correction parameter for rugosity is defined for each analyzed element as the ratio of the wt.% content measured from an unaltered smooth surface area (total 100 wt.%) over the wt.% content measured from a roughened surface (total below 100 wt.%). For the 30-keV-irradiated surface, the analytical total is close to 94 wt.% (see column "d" in Table 1) and the corresponding correction parameters are listed in column "ρ" of Table 1. Finally, the correction procedure confirms that both (Mg + Fe)/Si and O/Si ratios are slightly larger than those of the initial olivine. This result suggests the presence of excess MgO in the probed volume. The modal fraction of MgO, consistent with the chemical composition of the irradiated area (Table 1), is a few percent (i.e., 8.5 mol %

considering the (Mg + Fe)/Si ratio, and 4 mol % with the O/Si ratio). Given the 2- to 3-μm depth resolution, if this MgO-rich product forms a uniform layer onto the irradiated area, the thickness of this layer should range between 80 nm (4 vol.% of
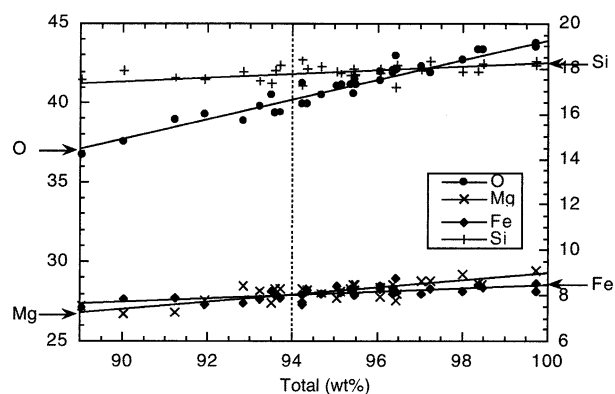

Fig. 8. EMP analyses of O ($\bullet$), Mg (x), Si (+), and Fe ($\blacklozenge$) (in weight percent) vs. the analytical total of an olivine, with surface roughened by polishing with abrasives. Expressions for the linear fits (solids lines) are $y = -18.38 + 0.6235x$ for O, $y = 7.129 + 0.2214x$ for Mg, $y = 1.26 + 0.0719x$ for Fe, and $y = 9.94 + 0.08357x$ for Si. Using the above linear fits, the correction parameters for rugosity are estimated for each element as the ratio of the wt.% content measured from an unaltered surface area (total 100%) divided by the wt.% content measured from a rough surface area (total below 100%). For the 30-keV-irradiated surface of the olivine, the average analytical total was found $\sim$94% (see column "d" in Table 1. The corresponding correction parameter for each analyzed element is given in column "ρ").

2 μm) and 300 nm (10 vol.% of 3 μm). In fact, EMP and SEM analyses performed on the cross-sections (Fig. 4) of the irradiated layer did not show the presence of such a layer, suggesting that the MgO excess does not form a uniform layer.

To summarize, irradiation by 30-keV electrons is only efficient with ferrous olivine, not with iron-free forsterite. A nanometer-sized silicate rim, richer in Si than the olivine, is deposited around the irradiated zone. A micrometer-sized layer, having a chemical composition close to that of the initial olivine and a strongly modified microstructure, is formed at the surface of the irradiated zone. By extension, such a process should produce two layers at the surfaces of irradiated ferrous silicates.

4. DISCUSSION

4.1. Damage Due to Electrostatic Discharges in the Dielectric Lattice

The rounded shapes of the structural damages caused to the irradiated surface of an iron-bearing olivine could result from melting related to elevated surface temperature and electrostatic effects. We verified that the required rise in temperature cannot be due to dissipation of the implanted energy as heat in the probed volume. The maximal temperature increase can be estimated, for a steady state and the electron microprobe beam at rest, by the following formula (Castaing, 1960):

$$\Delta T = \frac{3UI}{4\pi\lambda r} \qquad (1)$$

where λ is the thermal conductivity of olivine (4.89 $Wm^{-1}{}^{\circ}C^{-1}$ at room temperature; Guéguen and Palciauskas, 1992), I is the primary current (60 nA for this work), U is the accelerating voltage (30 kV), and r is the radius of the excited hemispherical volume. A value of ~2 μm was calculated with the noncommercial Monte Carlo SS_MC program, written by D. C. Joy in 1991. For our olivine specimen, the highest calculated temperature variation is ~40°C. A simple dissipation of the incident energy into heat cannot account for the observed damage. The melting point of an $(Mg_{0.89}Fe_{0.11})_2SiO_4$ olivine is 1720°C at 1 bar (Bowen and Schairer, 1935; Presnall 1995).

The irradiation by 30-keV electrons of shielded olivine produces a negative charge (Cazaux and Le Gressus, 1991; Cazaux, 1999). We propose that electrostatic discharges in the dielectric lattice of the olivine cause the observed damage. Electrostatic discharges occur where the voltage stress induced by accumulated charges exceeds the bulk breakdown strength of the olivine. The trapped charges are then released suddenly and the dielectric lattice breakdown occurs (Blaise and Le Gressus, 1992). The study of the coupling between the charge detrapping and the macroscopic damage, possibly the melting or the volatilization of olivine due to electron flows along few paths, is beyond the scope of this paper. The voltage stress induced in olivine by an implanted charge, q (C), stored at a fixed depth, d, below a surface, S, which potential is fixed arbitrarily at zero, can be calculated by the following equation:

$$\frac{U}{d} = \frac{q}{\kappa\varepsilon_0 S} \qquad (2)$$

where ε_o is the permittivity of vacuum and κ is the relative permittivity of olivine (7.71 along the [010] crystallographic axis at room temperature; Cygan and Lasaga, 1986). Assuming that, during one scan of the experiment #13 (see Table 2), the entire incident charge is implanted 2 μm below the irradiated surface, the calculated voltage stress is equal to 2.6 10^7 keV/cm. It is larger than the highest 10^3 keV/cm voltage strength reported for dielectrics. The relaxation time, τ_{Ol}^e, of such charged systems (Mulville, 1999) can be estimated by the expression:

$$\tau_{Ol}^e = \frac{\kappa\varepsilon_0}{\sigma} \qquad (3)$$

where σ is the electrical conductivity (10^{-13} Sm^{-1} for olivine at room temperature; Guéguen and Palciauskas, 1992). It is equal to ~10 min and bigger than the 30-s experimental period T. The interpretation of the observed damages as electrostatic discharge effects appears plausible. But respectively, the charge threshold q_c obtained by this model for the highest 10^3 keV/cm voltage strength is equal to 0.034 $pC\mu m^{-2}$ and less than all the Q charges of this study (Table 2), showing the limitations of this model. Real dielectrics contain heterogeneities such as dislocations, charges are implanted continuously within the first micrometers below the surface, and incident charges are not totally implanted.

Indeed, under the studied experimental conditions and simultaneously to the bulk charge process, irradiation by 30-keV electrons of shielded olivine induces the surface formation of an electrostatic mirror. This has also been observed with other dielectrics (Vallayer, 1995; Asokan, 2000). The mirror repels the electron beam and impedes the increase of the volume charge. The quantitative estimations of the voltage stress distribution and of its evolution during the experiment are thus more complex than discussed above. The two processes, the electrostatic discharges and the mirror formation processes, explain the observations only if (1) processes of charge relaxation destroy the electrostatic mirror, and if (2) the voltage stress increases with the quantity of implanted charge, the breakdown strength then corresponding to a threshold of implanted charge. Damage does not occur with very strong beam intensities and short scanning periods (experiments #2 and #3 in Table 2) because the fast formation of an electrostatic mirror makes it impossible to reach the critical discharge threshold. Also, damage does not happen for small beam intensities and long scanning periods because the trapped charge diffuses and the discharge threshold is never reached (experiments #4 and #5 in Table 2). When appropriate damage conditions are obtained, damage evolves along the discharging cycles as a function of the total deposited charge (Figs. 3 and 5). Finally, differences observed between iron-free and iron-bearing olivine are probably related to the differences between their electrical properties (Tyburczy and Fisler, 1995); the bandgap is 7.5 eV in iron-free forsterite and 3.3 eV in a natural 10% fayalite-containing olivine (Shankland, 1968). The appropriate damage conditions for Fe-bearing olivine must then be quite different than for forsterite.

4.2. Electrostatic Discharges as a Mechanism for Space Weathering

In the interplanetary medium of the solar system, electrons come mostly from the solar wind and are always associated with energetic cations, mainly protons and helium ions. Among the electronic population, 10-keV-range electrons compose (Krucker et al., 1999) the high-energy "super-halo" of the quasi-steady-state electron population of the solar wind, and an unknown amount is also emitted during the solar impulsive events (Lin et al., 1997). Mineralogical implications of the accumulation of 10-keV-range electrons cannot be easily estimated because neither the possible effect of interference and neutralization between the different particles of the solar wind nor a simple model of the variation of the electron flux of the solar wind are documented. However, negative charging of the exterior surfaces and electrostatic breakdowns do occur when spacecraft encounter a low-density plasma with energies from 1 to 50 keV as a geomagnetic substorm environment (Purvis et al., 1984). Electrons of a plasma have a larger velocity than protons because of their lower mass. This translates into a much higher net flux of electrons and into charging effects (Mulville, 1999). In addition, some evidence for negative charging of the lunar surface in shadow is established (Halekas et al., 2002). The exposure time required to accumulate 100 $pC\mu m^{-2}$, a typical value giving rise to the studied damage in olivine, can be estimated to be tens of years, considering the total average quasi-steady electron flux at 1 AU from the Sun (2–$2.5 \cdot 10^8$ $cm^{-2}s^{-1}$, Ko and Groth, 1999; Guhathakurta et al., 1999). Due to electron-rich solar impulsive events (Reames, 1990, 1997; Krucker et al., 1999), occurring several times per day, the electron flux, for a given energy, can momentarily increase by 10^5 (Lin et al., 1997). The exposure time previously calculated decreases then to a few hours. If the entire 10-keV range electrons are taken into account, this can result in accumulation times much smaller than the relaxation time in olivine τ_{Ol}^e. By comparison, the exposure time on the lunar surface of a 50-μm layer, which corresponds to the average grain size of dust, is a few thousand years (Kirsten et al., 1970; Quaide et al., 1970; Borg et al., 1980). Also the life times of dust particles generated from comets are of the order of 10^5 years (Brownlee, 1985). These characteristic times suggest that charge effects, such as those described in the present study, could be an important mechanism of space weathering in lunar regolith and in interplanetary dust particles.

In lunar grains, the microstructures attributed to space weathering are micrometer-long nuclear tracks (Bibring et al., 1972; Phakey et al., 1972; Phakey and Price, 1972) and amorphous rims (Anderson et al., 1970; Carter and MacGregor, 1970; McKay et al., 1970). Refined transmission electron microscopy (TEM) observations of the fine size fraction of lunar regolith revealed nanostructures within rims and the corresponding irradiated crystals (Keller and McKay, 1994; Bernatowicz et al., 1994). The nanostructures and chemical compositions of these rims were used to classify them (Keller and McKay, 1997). Two types of rims are predominant and are often superimposed. The "amorphous" rims are adjacent to the inner crystal, have an O/Si ratio similar to that of the bulk crystal, and formed in situ. The "inclusion-rich" rims are external, have an O/Si ratio lower than the bulk, and formed partly from indigenous material, although not entirely, because iron precipitates are observed around iron-free grains. Two main scenarios were proposed to explain their formation: (a) in situ amorphization due to sputtering caused by high-energy particles of solar wind, and (b) condensation of a gas phase that formed by volatilization of portions of rocks and soil grains during impacts of micrometeorites. At this level of description, some of these rims are indeed quite comparable to those produced in our study. Thus, a third explanation could be that a fraction of the rims observed in lunar regolith grains could have been formed in a single process due to space charging effects, as proposed here. In that case, a testable prediction of our experimental observations would be that the formation of such rims should be facilitated on insulating minerals having however relatively small bandgaps, such as ferrous olivine or ferrous pyroxenes, rather than on metal or on strongly insulating materials such as corundum and forsterite. Relationships between electrical conductivity and thickness of rims on different minerals or among one mineral with different compositions, such as pyroxene or olivine with different iron contents, should be examined to establish whether this mechanism is operating in the solar system and to what extent. TEM observations of the prepared samples should also be done to allow a more precise comparison with the rims observed on grains of the lunar regolith.

Associate editor: C. Koeberl

REFERENCES

Anderson A. T., Crewe A. V., Goldsmith J. R., Moore P. B., Newton J. C., Olsen E. J., Smith J. V., and Wyllie P. J. (1970) Petrologic history of Moon suggested by petrography, mineralogy, and crystallography. *Science* **167**, 587–589.

Asokan T. (2000) Ceramic dielectrics for space applications. *Current Sci. India* **79**, 348–351.

Bernatowicz T. J., Nichols R. H., and Hohenberg C. M. (1994) Vapor deposits in the lunar regolith: Technical comment. *Science* **264**, 1779–1780.

Bibring J. P., Duraud J. P., Durrieu L., Jouret C., Maurette M., and Meunier R. (1972) Ultrathin amorphous coatings on lunar dust grains. *Science* **175**, 753–755.

Blaise G. and Le Gressus C. (1992) Flashover in insulators related to the destabilization of a localized space charge. *Comptes Rend. Acad. Sci. II* **314**, 1017–1024.

Borg J., Chaumont J., Jouret C., Langevin Y., and Maurette M. (1980) Solar wind radiation damage in lunar dust grains and the characteristics of the ancient solar wind. In *Proc. Conf. Ancient Sun* (eds. R. O. Pepin, J. A. Eddy, and R. B. Merrill), pp. 431–461. *Geochim. Cosmochim. Acta Suppl.* 13. Pergamon Press, New York.

Bowen N. L. and Schairer J. F. (1935) The system MgO-FeO-SiO$_2$. *Am. J. Sci.* **29**, 151–217.

Bradley J. P. (1994) Chemically anomalous preaccretionally irradiated grains in interplanetary dust from comets. *Science* **265**, 925–929.

Bradley J. P., Germani M. S., and Brownlee D. E. (1989) Automated thin-film analyses of anhydrous interplanetary dust particles in the analytical electron microscope. *Earth Planet. Sci. Lett.* **93**, 1–13.

Brownlee D. E. (1985) Cosmic dust: Collection and research. *Annu. Rev. Earth Planet. Sci.* **13**, 147–173.

Carrez P., Leroux H., Cordier P., and Guyot F. (2001) Electron-irradiation-induced phase transformation and fractional volatilization in (Mg,Fe)$_2$SiO$_4$ olivine thin films. *Philosoph. Mag. A* **81**, 2823–2840.

Carter J. L. and MacGregor I. D. (1970) Mineralogy, petrology and surface features of lunar samples 100062,35, 10067,9, 10069,30, and 10085,16. *Science* **167**, 661–663.

Castaing R. (1960) Electron probe analysis. In *Advances in Electronics and Electron Physics,* Vol. 13 (eds. L. L. Marton and C. Marton), pp. 317–386. Academic Press, New York.

Cazaux J. (1999) Some considerations on the secondary electron emission, δ, from e-irradiated insulators. *J. Appl. Phys.* **85**, 1–11.

Cazaux J. and Le Gressus C. (1991) Phenomena relating to charge in insulators: Macroscopic effects and microscopic causes. *Scanning Microsc.* **5**, 17–27.

Crovisier J., Leech K., Bockelée-Morvan D., Brooke T. Y., Hanner M. S., Altieri B., Keller H. U., and Lellouch E. (1997) The spectrum of Comet Hale-Bopp (C/1995 01) observed with the Infrared Space Observatory at 2.9 astronomical units from the sun. *Science* **275**, 1904–1907.

Cygan R. T. and Lasaga A. C. (1986) Dielectric and polarization behavior of forsterite at elevated temperatures. *Am. Mineral.* **71**, 758–766.

Demyk K., Carrez P., Leroux H., Cordier P., Jones A. P., Borg J., Quirico E., Raynal P. I., and d'Hendecourt L. (2001) Structural and chemical alteration of crystalline olivine under low energy He+ irradiation. *Astron. Astrophys.* **368**, L38–L41.

Dukes C. A., Baragiola R. A., and McFadden L. A. (1999) Surface modification of olivine by H+ and He+ bombardment. *J. Geophys. Res.* **104**, 1865–1872.

Gong W. L., Wang L. M., and Ewing R. C. (1998) Cross-section transmission electron microscopy of irradiated-induced amorphization in α-quartz. *J. Appl. Phys.* **84**, 4204–4208.

Guéguen Y. and Palciauskas V. (1992) *Introduction à la physique des roches.* Hermann Press, Paris, pp. 1–299.

Guhathakurta M., Sittler E. C., and McComas D. (1999) Semi-empirical MHD model of the solar wind and its comparison with Ulysses. *Space Sci. Rev.* **87**, 199–206.

Halekas J. S., Mitchell D. L., Lin R. P., Hood L. L., Acuña M. H., and Binder A. B. (2002) Evidence for negative charging of the lunar surface in shadow. *Geophys. Res. Lett.* **29**, 1–4.

Hanner M., Lynch D. K., and Russel R. (1994) The 8–13 micron spectra of comets and the composition of silicate grains. *Astrophys. J.* **425**, 274–285.

Hiroi T. and Sasaki S. (2001) Importance of space weathering simulation products in compositional modeling of asteroids: 349 Dembowska and 446 Aeternitas as examples. *Meteoritics Planet. Sci.* **82**, 1587–1596.

Hochella M. F., Lindsay J. R., Mossoti V. G., and Eggleston C. M. (1988) Sputter depth profiling in mineral-surface analysis. *Am. Mineral.* **73**, 1449–1456.

Jessberger E. K., Christoforidis A., and Kissel J. (1988) Aspects of the major element composition of Halley's dust. *Nature* **332**, 691–695.

Karduck P. (1998) Quantitative near-surface microanalysis and depth profiling by EPMA. In *Modern Developments and Applications in Microbeam Analysis* (eds. G. Love, W. A. P. Nicholson, and A. Armigliato), pp. 109–123. *Mikrochim. Acta, Suppl. 15,* Springer-Verlag, New York.

Keller L. and McKay D. S. (1997) The nature and origin of rims on lunar soil grain. *Geochim. Cosmochim. Acta.* **61**, 2331–2341.

Keller L. P. and McKay D. S. (1994) Vapor deposits in the lunar regolith: Technical comment. *Science* **264**, 1780.

Kirsten T., Müller O., Steinbrunn F., and Zähringer J. (1970) Study of the distribution and variations of rare gases in lunar material by a microprobe technique. In *Proceeding of the 11th Lunar Science Conference, Geochim. Cosmochim. Acta Suppl. I, 2* (ed. A. A. Levinson), pp. 1331–1343. Pergamon Press, New York.

Ko Y. K. and Groth C. P. T. (1999) On the electron temperature and coronal heating in the fast solar wind constrained in-situ observations. *Space Sci. Rev.* **87**, 227–231.

Krucker S., Larson D., Lin R. P., and Thompson B. J. (1999) On the origin of impulsive electron events observed at 1 AU. *Astrophys. J.* **519**, 864–875.

Lemelle L., Guyot F., Fialin M., and Pargamin J. (2000) Experimental study of coupling between reduction and volatilization in olivine single crystals. *Geochim. Cosmochim. Acta.* **64**, 3237–3249.

Lin R. P., Larson D. E., Ergun R. E., McFadden J. P., Carlson C. W., Phan T. D., Ashford S., Anderson K. A., McCarthy M., Skoug R., Parks G. K., Reme H., Bosqued J. M., d'Uston C., Sanderson T. R., and Wenzel K.-P. (1997) Observation of the solar wind, the bow shock and upstream particles with the wind 3D plasma instrument. *Adv. Space Res.* **20**, 645–654.

McKay D. S., Grenwood W. R., and Morrison D. A. (1970) Morphology and related chemistry of small Lunar particles from tranquillity base. *Science* **167**, 654–656.

Mulville D. R. (1999) Avoiding problems caused by spacecraft on-orbit internal charging effects. *NASA Technical Handbook 4002*, Feb. 17, NASA Engineering Standards, Huntsville, pp. 1–45.

Phakey P. P. and Price P. B. (1972) Extreme radiation damage in soil from Mare Fecunditatis. *Earth Planet. Sci. Lett.* **13**, 410–418.

Phakey P. P., Hutcheon I. D., Rajan R. S., and Price P. B. (1972) Radiation effects in soils from five lunar missions. In *Proceeding of the 3rd Lunar Science Conference, Geochim. Cosmochim. Acta Suppl. 3,* Pergamon Press, New York, pp. 2905–2915.

Pieters C. M. (1998) Constraints on our view of the Moon II: Space weathering. *New Views of the Moon Workshop.* Lunar and Planetary Institute, abstract no. 6027.

Pouchou J. L. and Pichoir F. (1991) Quantitative analysis of homogeneous or stratified microvolumes applying the model "PAP". In *Electron Probe Quantification* (eds. K. F. J. Heinrich and D. E. Newbury), pp. 31–75. Plenum Press, New York.

Pouchou J. L. and Pichoir F. (1984) A new model for quantitative X-ray microanalysis. Part I: Application to bulk specimen. *Rech. Aerospatiale* **3**, 167–192.

Presnall D. C. (1995) Phase diagram of Earth-forming minerals. In *Mineral Physics and Crystallography, A Handbook of Physical Constants* (ed. T. Ahrens), pp. 248–268. AGU Reference Shelf 2, American Geophysical Union, Washington.

Purvis C. K., Garrett H. B., Whittlesey A. C., Stevens N. J. (1984) Design guidelines for assessing and controlling spacecraft charging effects. *NASA Technical Paper 2361*, NASA Lewis Research Center, Cleveland, pp. 1–44.

Quaide W., Bunch T., and Wrigley R. (1970) Impact metamorphism of lunar surface materials. *Science* **167**, 671–672.

Reames D. V. (1999) Particle acceleration at the Sun and in the heliosphere. *Space Sci. Rev.* **90**, 413–491.

Reames D. V. (1997) Energetic particles and the structure of coronal mass ejections. In *Coronal Mass Ejections* (eds. N. Crooker, J. A. Jocelyn, and J. Feynman), pp. 217–226. Geophysical Monograph 99, American Geophysical Union, Washington, DC.

Reames D. V. (1990) Energetic particles from impulsive solar flares. *Astrophys. J.* **73**, 235–251.

Sasaki S., Nakamura K., Hamabe Y., Kurahashi E., and Hiroi T. (2001) Production of iron nanoparticles by laser irradiation in a simulation of lunar-like space weathering. *Nature* **410**, 555–557.

Shankland T. J. (1968) Band gap of forsterite. *Science* **161**, 51–53.

Tyburczy J. A. and Fisler D. K. (1995) Electrical properties of minerals and melts. In *Mineral Physics and Crystallography, A Handbook of Physical Constants* (ed. T. Ahrens), pp. 209–217. AGU Reference Shelf 2, American Geophysical Union, Washington.

Vallayer B. (1995) Modelisation of both electronic trajectories and electric field distribution in the vacuum near a trapped charge implanted with an electron beam. *Vide* **275**, 619–625.

Vance E. R., Cann C. D., and Richardson P. G. (1986) Electron irradiation-induced amorphism of some silicates. *Radiat. Eff. Lett.* **98**, 71–81.

Wang L. M., Eby R. K., Janeczek J., and Ewing R. C. (1991) In situ TEM study of the ion-beam induced amorphization of complex silicate structures. *Nucl. Instrum. Methods* **B59/60**, 395–400.

Willich P. and Wishmann U. (1998) Quantitative analysis of BN. (C, O, Ar, H)-coatings using EPMA and SIMS. In *Modern Developments and Applications in Microbeam Analysis* (eds. G. Love, W. A. P. Nicholson, and A. Armigliato), pp. 141–147. *Mikrochim. Acta, Suppl. 15,* Springer-Verlag, New York.

Wooden D. H., Harker D. E., Woodward C. E., Butner H. M., Koike C., Witteborn F. C., and McMurty C. W. (1999) Silicate mineralogy of the dust in the inner coma of comet C/1995 01 (Hale-Bopp) pre and postperihelion. *Astrophys. J.* **517**, 1034–1058.